Mechatronics 98 (2024) 103134

Contents lists available at ScienceDirect

Mechatronics

journal homepage: www.elsevier.com/locate/mechatronics

Underwater autonomous orientation using submarine light intensity gradient

Pengwei Hu [a], Wenbin Liu [b], Jian Yang [b,*], Xiang Yu [b], Lijun Xu [a], Lei Guo [b]

[a] School of Instrumentation and Optoelectronic Engineering, Beihang University, 37 Xueyuan Rd., Haidian District, Beijing, 100191, China
[b] School of Automation Science and Electrical Engineering, Beihang University, 37 Xueyuan Rd., Haidian District, Beijing, 100191, China

ARTICLE INFO

Keywords:
Underwater autonomous navigation
Underwater light field
Light intensity gradient
Integrated navigation system
Polarization navigation

ABSTRACT

It is a huge challenge for autonomous underwater vehicles (AUVs) to determine heading autonomously without the signal of satellite or underwater acoustic positioning system. The underwater polarization navigation is a newly-developed solution for self-orientation. However, the polarization navigation depending on the Rayleigh scattering model is susceptible to the multiple scattering induced by water depth. To address this issue, the underwater light intensity field is exploited benefiting from its environment suitability. By means of calculating the gradient of light intensity, a vector-field model, with resemblance to the ideal Rayleigh model in geometry, can be established for solar-tracking. The integrated navigation model is built based on the solar vector estimated by light intensity gradient (LIG) and inertial navigation system for heading determination. The static test in water tank and dynamic sea trial were conducted to validate the effectiveness of the LIG-based solar-tracking and orientation method, respectively.

1. Introduction

Autonomous underwater vehicles (AUVs) have broad application prospects in marine environment monitoring, resource exploration [1], et al. The navigation system is one of the critical components to guarantee the underwater task for AUV. Currently, the inertial navigation system (INS) has been an indispensable navigation means [1]. Due to the error accumulation over time for long-durance tasks, the aiding navigation is apparently necessary to correct INS errors. Global navigation satellite system (GNSS) is widely used to integrate with INS [2]. However, the shielding effect of water on the GNSS signal disables it underwater. Water acoustic positioning system is the unique strategy for underwater navigation [3]. The transponders placement limits the system application. The geophysical fields (e.g., geomagnetic field [4], gravitational field [5], and terrain [6]) rely on the prior data bank, which may not be available for unknown sea areas and unstructured underwater environment. The Doppler Velocity Log (DVL) [7] and optical flow [8,9] are employed autonomously for velocity measurement, but they are not applicable for attitude determination. In consequence, an autonomous navigational method without depending on prior knowledge is a significant challenge for underwater environment.

The submarine light field including light intensity and polarization (POL) field can be perceived by mantis shrimps [10,11] and trouts [12] for self-orientation. The POL field contains the information of solar position [13] which can be used for orientation by these aquatic animals. It is a key problem to estimate solar position in the POL-based navigation [14–16]. The solar position can be used for heading [17], attitude determination [16,18], and geolocalization [19]. The bio-inspired underwater POL navigation owns the advantages of autonomy, free of error accumulation, and prior knowledge independence. Thus, it becomes a viable option of underwater orientation [19,20] or aiding INS [21]. The underwater polarization field is divided into two portions by Snell's window induced by refraction. Powell, et al. have proposed a solar-tracking method using the outside underwater polarization field [19]. Nevertheless, the dark light intensity of the outside field reduces the polarization perception accuracy, deteriorating the solar-tracking performance. To tackle this problem, the inside polarization field, as a brighter one, has been exploited for underwater solar-tracking improvement [22].

Within the existing schemes, the refraction is treated as a dominant factor, while the water scattering is negligible under shallow water. Focusing on deeper environment, however, the water scattering cannot be omitted. The POL pattern of the ideal single-scattering Rayleigh model is symmetry. However, there are discrepancies between the real POL pattern and the ideal one, such as the non-vertical errors [23]. Multiple scattering in the air causes the symmetry of POL pattern breaking [24]. Especially for the underwater environment, the stronger multiple scattering of water breaks the POL pattern symmetry more seriously. This leads to constant deviations of the solar position estimation. On the other hand, the degree of polarization (DoP) in deep

* Corresponding author.
E-mail addresses: hupengwei@buaa.edu.cn (P. Hu), wb2103@buaa.edu.cn (W. Liu), jyang_buaa@buaa.edu.cn (J. Yang), xiangyu_buaa@buaa.edu.cn (X. Yu), lijunxu@buaa.edu.cn (L. Xu), lguo@buaa.edu.cn (L. Guo).

https://doi.org/10.1016/j.mechatronics.2023.103134
Received 29 June 2023; Received in revised form 7 September 2023; Accepted 21 December 2023
Available online 3 January 2024

water is low. Low DoP decreases the signal-to-noise ratio of the angle of polarization (AoP) acquisition, thereby affecting the accuracy of solar-tracking. Hence, the POL pattern is easily affected by multiple scattering as the depth increasing, and difficult to obtain with high accuracy.

The submarine light intensity is a more visual optical information that has not yet been exploited. The light intensity field is a scalar field that contains less spatial information than POL field. Notwithstanding, as well as the POL field, the light intensity field is formed by scattering of sunlight. It can be speculated that the light intensity field is an alternative source for solar-tracking. On celestial hemisphere, it is obvious that the farther away from the sun, the weaker the light intensity. The light intensity decreases with the increase of the scattering angle. Therefore, the direction of the maximum change of light intensity points towards the sun. Thus, the gradient of light intensity field can be exploited for the solar position estimation. The scalar field is subsequently transformed to be vector field by gradient calculation.

The mapping relationship of light intensity field and the solar position in the air is still applied to water environments. As compared with the POL field, the light intensity performs more robust under water refraction and multiple scattering. Additionally, the original light intensity is stronger than the polarization light intensity which is filtered by the polarizer. Therefore, in any underwater environment where the polarization field can be obtained, the light intensity field can certainly be obtained as well, even better. In consequence, the light intensity gradient (LIG) has the potential for solar-tracking improvement in the water scenario. The gradient of the DoP in the air has been proposed for navigation [25]. However, the multiple scattering depolarizes the underwater light so that the DoPs in the view field are generally low. The DoP distinction cannot be recognized by the polarimeter.

In this paper, an underwater solar-tracking method based on submarine light intensity gradient is proposed. The solar position estimation accuracy can be improved benefited from the robustness of the light intensity field in deep water. On this basis, the integrated navigation model of LIG/INS is established based on the solar vector. An underwater integrated navigation system is designed and thereby applied for underwater experiments. The statics and dynamic experiments are conducted to verify the improvements of LIG-based solar-tracking and self-orientation, as compared with the POL-based method, respectively. The main contributions of this work are summarized as follows:

1. A novel strategy that exploits submarine light intensity for underwater navigation is proposed. The light intensity is more robust comparing with the POL field under the effect of water multiple scattering in optical mechanism. Benefiting from the robustness of submarine light intensity, the solar-tracking accuracy can be improved via calculating gradient. Especially for deeper water environments, the constant deviations of solar-tracking arising from multiple scattering in POL-based method [22] can be eliminated significantly by exploiting LIG field.
2. A LIG model is represented and built using submarine light intensity for solar vector estimation. The vectors in LIG model follow the vertical relationship with solar vector which is less susceptible to environment. The traditional POL-based solar-tracking method [15,16,22] regards the measured POL field as an idea Rayleigh model without considering the model errors. Thus, compared to the traditional POL-based method, a more accurate solar vector can be estimated based on the robust geometrical relationship of LIG model.

2. Solar-tracking using submarine light intensity gradient

The light intensity decreases as the scattering angle increases. The scattering angle is equivalent to the angle between the solar vector and the observation vector (see Fig. 1(a)). If the concentric circles on the celestial hemisphere with the solar vector as the axis are created, the light intensity of any observation point on one concentric circle varies along the radial direction. Thus, the directions of the maximum change rate of light intensity, i.e., the light intensity gradients, orientate in accordance with the sun.

A brief theoretical analysis can be given as follows. The Rayleigh scattering can be expressed by Stokes vector $\boldsymbol{S}$ and Mueller matrix $\boldsymbol{M}$ as [26]

$$\begin{aligned}\boldsymbol{S}_1 &= \begin{bmatrix} I_1 \\ Q_1 \\ U_1 \\ V_1 \end{bmatrix} = \boldsymbol{M}\boldsymbol{S}_0 \\ &= \frac{1}{2}\left(\frac{e^2}{mc^2 R}\right)\begin{bmatrix} 1+\cos^2\theta & \sin^2\theta & 0 & 0 \\ \sin^2\theta & 1+\cos^2\theta & 0 & 0 \\ 0 & 0 & 2\cos\theta & 0 \\ 0 & 0 & 0 & 2\cos\theta \end{bmatrix}\begin{bmatrix} I_0 \\ Q_0 \\ U_0 \\ V_0 \end{bmatrix}.\end{aligned} \tag{1}$$

where $\boldsymbol{S}_0$ and $\boldsymbol{S}_1$ are the Stokes vectors of incident and scattering light, respectively, θ denotes the scattering angle, $e^2/mc^2 mc^2 (= 2.82 \times 10^{-13}$ cm) is the classical radius of an electron, and R is the distance of the observation point from the origin of the coordinate system. The coefficients in front of the matrix are regarded as a constant value k. The first element I in Stokes vector is light intensity. The scattering light intensity can be described as

$$I_1 = k\left(1+\cos^2\theta\right) I_0 + k\sin^2\theta Q_0 \tag{2}$$

If it is the single-scattering, $\boldsymbol{S}_0 = \begin{bmatrix} 1 & 0 & 0 & 0 \end{bmatrix}^T$. Thus the scattering light intensity is expressed as

$$I_1 = k\left(1+\cos^2\theta\right) I_0. \tag{3}$$

It shows that the scattering light intensity varied with scattering angle. When the multiple-scattering occurs, Q_0 is not equivalent to zero. However, owing to $Q_0 < I_0$, I_0 can be written as $I_0 = I_0' + Q_0$. Thus, we have

$$I_1 = k\cos^2\theta I_0' + k(1+Q_0), \tag{4}$$

which is also varied with scattering angle. Subsequently, the distribution of light intensity exhibits a pattern that depends on scattering angle. The influence of water depth on light intensity is mainly reflected in the weakening of the overall absolute light intensity, but the relative distribution pattern is not changed much. This characteristic of light intensity enables LIG-based solar-tracking to perform more stably than the POL-based one in deep water. Therefore, the LIG can be exploited for solar-tracking in this work.

The coordinate frame involved in this paper are defined as follows:

Body frame (*b*) [27]
- the x-axis is the right side of the object;
- the y-axis is the front side of the object;
- the z-axis is the upward side of the object.

Navigation frame (*n*) [27]
- the x-axis points to the local east;
- the y-axis points to the local north;
- the z-axis points to the opposite gravity.

Calculated navigation frame (*n'*) [27]
- the x-axis points to the local east with misalignment angles of INS;
- the y-axis points to the local north with misalignment angles of INS;
- the z-axis points to the opposite gravity with misalignment angles of INS.

Horizontal frame (*h*)
- h-frame is an intermediate frame from b-frame to n-frame;
- the z-axis points to the opposite gravity;
- the angle between x_h and x_n is the heading of the carrier.

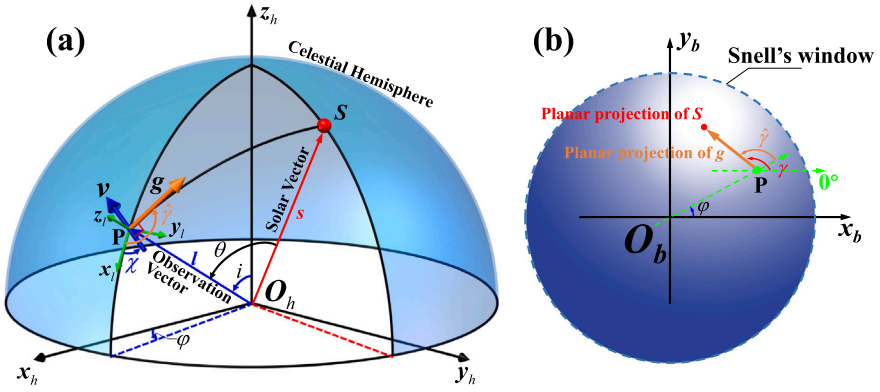

Fig. 1. Illustration of the vectors and angles involved in this work.

Light frame (l) [22]

- the z-axis points outward along the incident ray;
- the x-axis points downward along the tangential direction of the meridian line at the observation point on the celestial hemisphere;
- the y-axis is formed as a right-handed coordinate system.

The raw data acquired by the camera-based polarimeter is the light intensity that filtered by four directional polarizers, i.e., 0°, 45°, 90°, and 135°. The four polarization intensity images are denoted as $\boldsymbol{I}_0$, $\boldsymbol{I}_{45}$, $\boldsymbol{I}_{90}$, and $\boldsymbol{I}_{135}$. The light intensity image ($\boldsymbol{I}$) can be calculated as

$$\boldsymbol{I} = (\boldsymbol{I}_0 + \boldsymbol{I}_{45} + \boldsymbol{I}_{90} + \boldsymbol{I}_{135})/2. \tag{5}$$

It should be noted that the camera-based polarimeter is not required for the LIG-based solar-tracking. An ordinary camera is sufficient for the proposed method. The use of a camera-based polarimeter is intended for comparison between the LIG-based method and the POL-based method, for which the camera-based polarimeter is necessary.

The 2-D media filter algorithm is adopted to reprocess $\boldsymbol{I}$ firstly. Thus, the reprocessed 2-D image is used for gradient calculation. Consequently, the LIG of each pixel in $\boldsymbol{I}$ is represented by the gradient vector magnitude and the angle (γ) between the gradient vector and zero position of $\boldsymbol{I}$. The LIG vectors in the following context are regarded as unit vectors. γ is defined as LIG angle. Fig. 1(b) shows the LIG vector (orange vector) and LIG angle of one observation point (**P**) inside Snell's window.

The mapping from the 3-D real space to the 2-D image is nonlinear. Therefore, all the gradient vectors of $\boldsymbol{I}$ cannot intersect at on point. The solar position estimation based on the intersection is unreasonable. The 3-D LIG vectors as shown in Fig. 1(a) should be restored from the 2-D LIG angles.

Only the pixels inside Snell's window are available for solar-tracking. It can be calculated by the attitude of the integrated navigation system and lens model ($\boldsymbol{\Theta}$) that is calibrated in advance by OCamCalib Toolboxs [28]. The attitude of the navigation system is presented by direction cosine matrix (DCM) from b-frame to h-frame ($\boldsymbol{C}_b^h$). The observation vector in h-frame ($\boldsymbol{l}^h$) of one pixel with the coordinate (m, n) is

$$\boldsymbol{l}^h = \boldsymbol{C}_b^h \boldsymbol{\Theta}(m, n). \tag{6}$$

Thus, the refraction angle (r) is

$$r = \arctan\left(\frac{\sqrt{(\boldsymbol{l}^h(1))^2 + (\boldsymbol{l}^h(2))^2}}{\boldsymbol{l}^h(3)}\right), \tag{7}$$

where $\boldsymbol{l}^h(*)$ represents the $*$-th factor of $\boldsymbol{l}^h$.

If $r \le \arcsin(n_a/n_w)$, the corresponding pixel (m, n) is judged as a in-window one which can be used for solar-tracking.

It can be seen in Fig. 1(a), for any observation point, the gradient vector ($\boldsymbol{g}$), observation vector ($\boldsymbol{l}$), and solar vector ($\boldsymbol{s}$) are coplanar. Every pixel can determine a plane. Therefore, the solar vector can be estimated via the intersection of the planes determined by two or more pixels. The unit normal vector ($\boldsymbol{v}$) of a plane is adopted to present the plane. Every $\boldsymbol{v}$ is vertical to $\boldsymbol{s}$. Thus, the solar vector estimation based on planes intersection is transformed to be the cross-produce of two normal vectors. $\boldsymbol{v}$ in l-frame is represented as

$$\boldsymbol{v}^l = \begin{bmatrix} \cos\chi & \sin\chi & 0 \end{bmatrix}^T, \tag{8}$$

where χ is the angle from $\boldsymbol{x}_l$ to $\boldsymbol{v}$. On account of the bidirectionality of the normal vector, the range of χ is $[-90°, 90°]$. Thus, χ can be calculated as

$$\chi = \arctan(\tan(\hat{\gamma} - 90)), \tag{9}$$

where $\hat{\gamma} = \gamma - \varphi$ (see Fig. 1(b)). φ is the azimuth of the pixel (m, n), which can be calculated by the pixel coordinate.

The DCM from l-frame to h-frame can be given as

$$\boldsymbol{C}_l^h = \begin{bmatrix} \cos i\cos\varphi & -\sin\varphi & \sin i\cos\varphi \\ \cos i\sin\varphi & \cos\varphi & \sin i\sin\varphi \\ -\sin i & 0 & \cos i \end{bmatrix}. \tag{10}$$

where i is the incident angle that can be deduced by Snell's law

$$i = \arcsin\left(\frac{n_w \sin r}{n_a}\right). \tag{11}$$

Remark 1. The refraction compensation is completed by Eqs. (10) and (11). In the POL-based solar-tracking, as the polarized light is represented by a vector (i.e., E-vector), the refraction is compensated from two aspects [22]. One is the bending of the ray following Snell's law, and the other one is the deflection of the POL plane governed by Fresnel refraction equations [29]. Herein only the bending of the ray need to be considered owing to the light intensity is scalar. The process of calculation is simplified and the calculated errors are avoided partly.

Thus, the normal vector in h-frame is expressed as

$$\boldsymbol{v}^h = \boldsymbol{C}_l^h \boldsymbol{v}^l = \begin{bmatrix} \cos i\cos\varphi - \sin\varphi\sin\chi \\ \cos i\sin\varphi\cos\chi + \cos\varphi\sin\chi \\ -\sin i\cos\chi \end{bmatrix}. \tag{12}$$

In the ideal Rayleigh model, the E-vector is vertical to the solar vector. Here the intermediate vector of $\boldsymbol{v}$ is also vertical to the solar vector. Thus, $\boldsymbol{v}$ calculated by LIG is equivalent to the E-vector of POL in the ideal Rayleigh model. The intermediate vector field on the celestial hemisphere is defined as LIG model. By this means, the LIG model, with resemblance to the ideal Rayleigh model, is established as an intermediate model for solar-tracking.

Remark 2. Previous works regard the celestial polarization field as the single-scattering Rayleigh model [22]. The vertical relationship is used for solar-tracking. The real celestial POL field, however, is not strictly

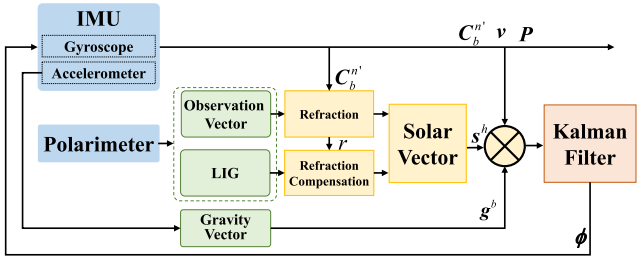

Fig. 2. Flowchart of the underwater integrated navigation model.

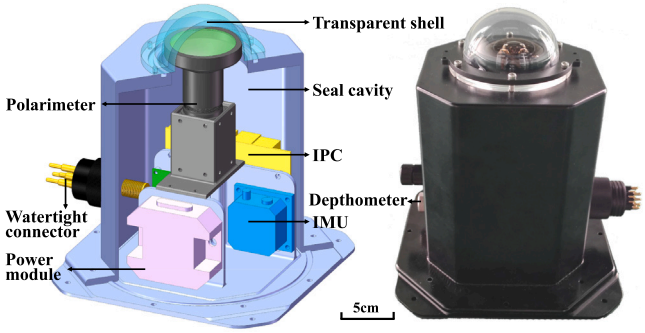

Fig. 3. The design sketch and internal components of the underwater integrated navigation system.

consistent with the ideal model due to the complex optical effects other than Rayleigh scattering. This model approximation causes the solar-tracking errors. In this work, a LIG model is established using light intensity as an intermediate model for solar-tracking. It is more aligned with the vertical relationship when compared with the real celestial POL field from the perspective of geometrical relationship. The non-vertical errors in the measured POL field can be eliminated significantly by LIG model.

The unit normal vectors of all the available pixels are written in a matrix as

$$\boldsymbol{V} = \begin{bmatrix} \boldsymbol{v}_1^h & \boldsymbol{v}_2^h & \cdots & \boldsymbol{v}_n^h \end{bmatrix}_{3\times N} \tag{13}$$

where N is the number of the available pixels. The solar vector in h-frame can be optimally estimated by minimizing the deviation as

$$\boldsymbol{L}(\boldsymbol{s}^h, \kappa) = \boldsymbol{s}^{hT}\boldsymbol{V}^h\boldsymbol{V}^{hT}\boldsymbol{s}^h - \kappa(\left\|\boldsymbol{s}^h\right\| - 1), \tag{14}$$

where κ is the Lagrange multiplier. $\partial \boldsymbol{L}/\partial \boldsymbol{s}^h = 0$ leads to

$$\kappa \boldsymbol{s}^h = \boldsymbol{V}^h\boldsymbol{V}^{hT}\boldsymbol{s}^h. \tag{15}$$

Thus, the solar vector ($\boldsymbol{s}^h$) is the eigenvector of the matrix ($\boldsymbol{V}^h\boldsymbol{V}^{hT}$) corresponding to the minimum eigenvalue κ_{min} [15]. Both $\boldsymbol{s}^h$ and $-\boldsymbol{s}^h$ meet Eq. (11). The ambiguity of solar vector is eliminated by light intensity. Take the first two elements of $\boldsymbol{s}^h$ and $-\boldsymbol{s}^h$ as the corresponding 2-D projection vectors ($\boldsymbol{s}_p$ and $-\boldsymbol{s}_p$). The 2-D projection vector of solar vector points to the area with higher light intensity. By means of comparing the average light intensity of the two areas pointed to by $\boldsymbol{s}_p$ and $-\boldsymbol{s}_p$, the solar vector can be determined.

3. Orientation by integrated navigation system based on solar vector

The integrated navigation model is established based on the solar vector with INS for orientation. The integration architecture is illustrated in Fig. 2.

3.1. System state model

The system state vector is represented as

$$\boldsymbol{X} = [\boldsymbol{\phi}, \delta\boldsymbol{v}, \delta\boldsymbol{p}, \boldsymbol{\epsilon}, \boldsymbol{\nabla}]^T, \tag{16}$$

where $\boldsymbol{\phi} = [\phi_E, \phi_N, \phi_U]$ are misalignment angles; $\delta\boldsymbol{v} = [\delta v_E, \delta v_N, \delta v_U]^T$ are velocity errors; $\delta\boldsymbol{p} = [\delta L, \delta\lambda, \delta h]^T$ are errors of latitude, longitude and height, respectively. $\boldsymbol{\epsilon} = [\epsilon_E, \epsilon_N, \epsilon_U]^T$ are gyroscope drift rates; $\boldsymbol{\nabla} = [\nabla_E, \nabla_N, \nabla_U]^T$ denote accelerometer bias. The system state equation [30] can be expressed as

$$\dot{\boldsymbol{X}} = \boldsymbol{\Phi}\boldsymbol{X} + \boldsymbol{W}, \tag{17}$$

where $\boldsymbol{\Phi}$ is the system matrix, $\boldsymbol{W}$ is the system noise and $\boldsymbol{W} \sim \mathcal{N}(0, \boldsymbol{Q})$. $\boldsymbol{Q}$ is the covariance matrix of the state noise.

3.2. System measurement model based on gravity vector

The gravity vector is adopted to correct the horizontal attitude. Owing to that the AUV underwater movement is nearly stable in low acceleration situations, the gravity vector in b-frame ($\boldsymbol{g}^b$) can be calculated by the three-axis accelerometer. The measurement equation based on gravity vector is expressed as

$$\begin{aligned} \boldsymbol{Z}_g &= \boldsymbol{C}_b^{n'}(\boldsymbol{g}^b + \delta\boldsymbol{g}) - \boldsymbol{g}^n \\ &\approx (\boldsymbol{I} - \boldsymbol{\phi}\times)\boldsymbol{C}_b^n(\boldsymbol{g}^b + \delta\boldsymbol{g}) - \boldsymbol{g}^n, \\ &= (\boldsymbol{g}^n\times)\boldsymbol{\phi} + \boldsymbol{C}_b^{n'}\delta\boldsymbol{g} \end{aligned} \tag{18}$$

where $\boldsymbol{g}^n = [0, 0, -9.8]^T$ is the gravity vector is n-frame and $\delta\boldsymbol{g}$ is the measurement noise of gravity vector. Thus, the measurement equation can be rewritten as

$$\boldsymbol{Z}_g = \boldsymbol{H}_g\boldsymbol{X} + \boldsymbol{V}_g \tag{19}$$

where $\boldsymbol{H}_g = \begin{bmatrix} (\boldsymbol{g}^n\times) & \boldsymbol{O}_{3\times 12} \end{bmatrix}$, $\boldsymbol{V}_g = \boldsymbol{C}_b^{n'}\delta\boldsymbol{g}$ and $\boldsymbol{V}_g \sim \mathcal{N}(0, \boldsymbol{R}_g)$. $\boldsymbol{R}_g$ is the covariance matrix of the measurement noise of the gravity vector.

Kalman filter is used to estimate $\boldsymbol{\phi}$. The coordinate frame updated by the estimated $\boldsymbol{\phi}$ is defined as n^*, Due to the limitations of the gravity vector, it can only correct the horizontal attitude but not the heading. Thus, there are still misalignment angles between n^*-frame and n-frame, which is denoted as $\boldsymbol{\phi}^* = [\phi_E^*, \phi_N^*, \phi_U^*]$. The heading after the correction of $\boldsymbol{\phi}^*$ is represented as ψ^*. Thus the relationship between $\boldsymbol{C}_b^{n*}$ and $\boldsymbol{C}_b^h$ can be written as

$$\boldsymbol{C}_b^{n*} = \boldsymbol{C}_h^{n*}\boldsymbol{C}_b^h = \begin{bmatrix} \cos\psi^* & \sin\psi^* & 0 \\ -\sin\psi^* & \cos\psi^* & 0 \\ 0 & 0 & 1 \end{bmatrix}\boldsymbol{C}_b^h. \tag{20}$$

$\boldsymbol{C}_b^h$ can be calculated by the three third-line factors in $\boldsymbol{C}_b^{n*}$. Generally, the data updated frequency of INS is higher than that of the camera-based polarimeter. Therefore, if the polarimeter is not updated, $\boldsymbol{C}_b^{n*}$ is used as the initial value for the measurement update of the next time. Otherwise, $\boldsymbol{C}_b^h$ is used for solar vector estimation as shown in Eq. (6).

3.3. System measurement model based on solar vector

When the polarimeter is updated, $\boldsymbol{s}^h$ is obtained as described in Section 2. $\boldsymbol{s}^{n*}$ can be given as

$$\boldsymbol{s}^{n*} = \boldsymbol{C}_h^{n*}\boldsymbol{s}^h = \begin{bmatrix} \cos\psi^* & \sin\psi^* & 0 \\ -\sin\psi^* & \cos\psi^* & 0 \\ 0 & 0 & 1 \end{bmatrix}\boldsymbol{s}^h. \tag{21}$$

The solar vector in n-frame ($\boldsymbol{s}^n$) can be calculated by solar ephemeris [31]. The relationship between $\boldsymbol{s}^n$ and $\boldsymbol{s}^{n*}$ is expressed as

$$\boldsymbol{s}^{n*} = \boldsymbol{C}_n^{n*}\boldsymbol{s}^n \approx (\boldsymbol{I} - \boldsymbol{\phi}^*\times)\boldsymbol{s}^n. \tag{22}$$

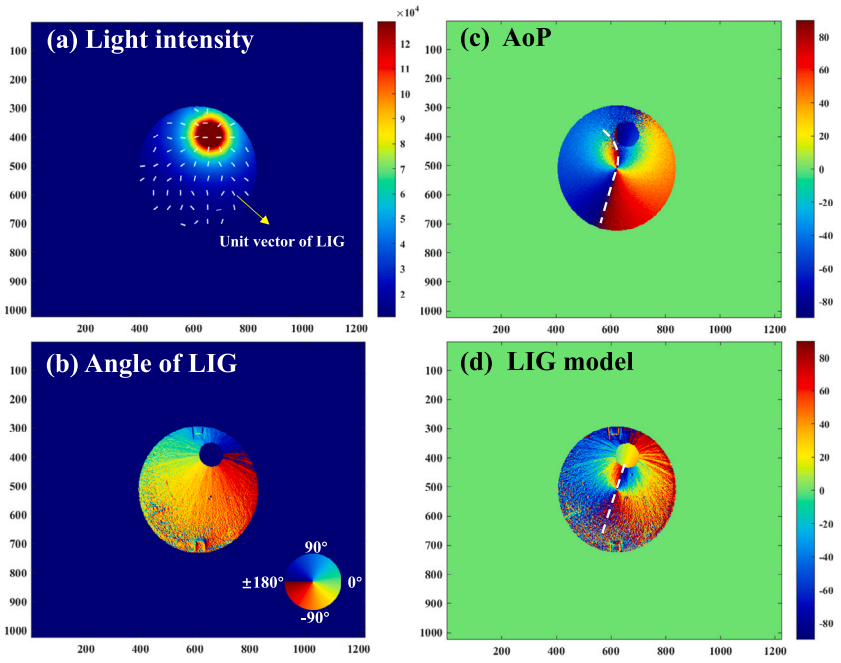

Fig. 4. An example of the light intensity pseudocolor and the LIG model of underwater light field in the static experiment.

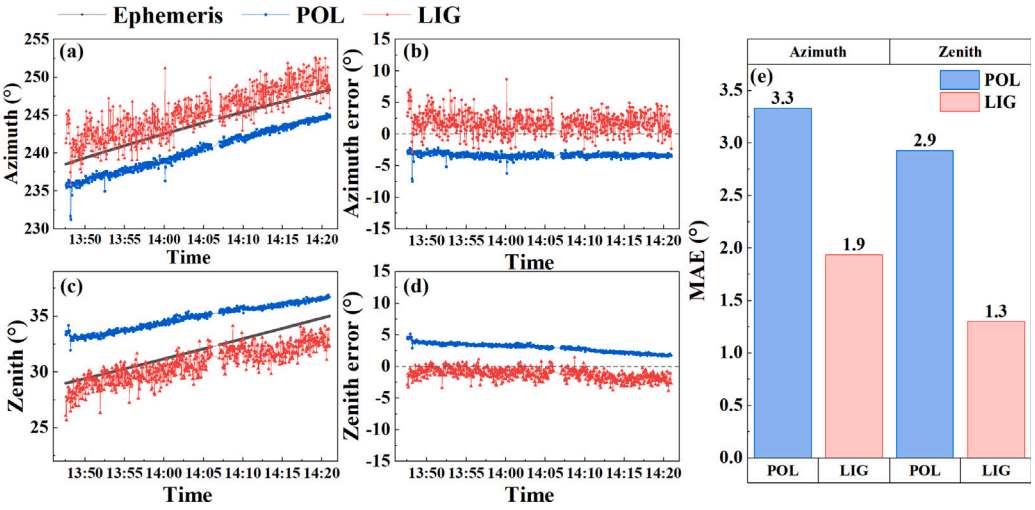

Fig. 5. The solar-tracking comparison between the POL-based and the LIG-based methods in the static experiment.

Thus, we have

$$\boldsymbol{s}^{n*} - \boldsymbol{s}^{n} = (\boldsymbol{s}^{n}\times)\boldsymbol{\phi}^{*}. \tag{23}$$

Considering the measurement noise of the solar vector ($\delta\boldsymbol{s}$), $\boldsymbol{s}^{n*} = \boldsymbol{C}_{h}^{n*}(\hat{\boldsymbol{s}}^{h} - \delta\boldsymbol{s})$, where $\hat{\boldsymbol{s}}^{h}$ represents the solar vector estimated by LIG. By letting $\boldsymbol{Z}_{s} = \boldsymbol{C}_{h}^{n*}\hat{\boldsymbol{s}}^{h} - \boldsymbol{s}^{n}$, and $\boldsymbol{V}_{s} = \boldsymbol{C}_{h}^{n*}\delta\boldsymbol{s}$, the measurement equation based on solar vector can be rendered as

$$\boldsymbol{Z}_{s} = \boldsymbol{H}_{s}\boldsymbol{X} + \boldsymbol{V}_{s}, \tag{24}$$

where $\boldsymbol{H}_{s} = [\ (\boldsymbol{s}^{n}\times)\quad \boldsymbol{O}_{3\times12}\ ]$ and $\boldsymbol{V}_{s} \sim \mathcal{N}(0, \boldsymbol{R}_{s})$. $\boldsymbol{R}_{s}$ is the covariance matrix of the measurement noise of the solar vector.

Kalman filter is used to estimate ϕ_{U}^{*}, and the heading can be obtained subsequently after correction. In Kalman filter, the initial state covariance matrix ($\boldsymbol{P}_{0}$), the covariance matrixes of the state noise ($\boldsymbol{Q}$) and measurement noise ($\boldsymbol{R}_{g}$ and $\boldsymbol{R}_{s}$) are key parameters. As far as the authors know, there is no systematic approach of determination of the parameters. In this paper, they are determined by trial-and-error tests. They are selected as follows

$$\begin{aligned}
\boldsymbol{P}_{0} &= diag([0.5^{\circ}; 0.5^{\circ}; 0.5^{\circ}; 1\ \text{m/hr}; 2^{\circ}/\text{hr}; 2^{\circ}/\text{hr}; 10\ \mu\text{g}; 10\ \mu\text{g}; 10\ \mu\text{g}])^{2},\\
\boldsymbol{Q} &= diag([0.01^{\circ}/\sqrt{\text{hr}}; 0.01^{\circ}/\sqrt{\text{hr}}; 0.16^{\circ}/\sqrt{\text{hr}};\\
&\quad 5\ \mu\text{g}/\sqrt{\text{Hz}}; 5\ \mu\text{g}/\sqrt{\text{Hz}}; 5\ \mu\text{g}/\sqrt{\text{Hz}}; 0; 0; 0; 0; 0; 0; 0; 0; 0])^{2},\\
\boldsymbol{R}_{g} &= diag([0.1\ \text{g}; 0.1\ \text{g}; 0.1\ \text{g}])^{2},\\
\boldsymbol{R}_{s} &= diag([0.05; 0.05; 0.05])^{2}.
\end{aligned}$$

4. Underwater experiments and results

In this section, the static test in water tank and dynamic sea trial were conducted to evaluate the performances of the proposed LIG-based solar-tracking and orientation, respectively. The performances of these two methods are compared to verify the benefits of the developed one in the deep water where the multiple scattering is severer.

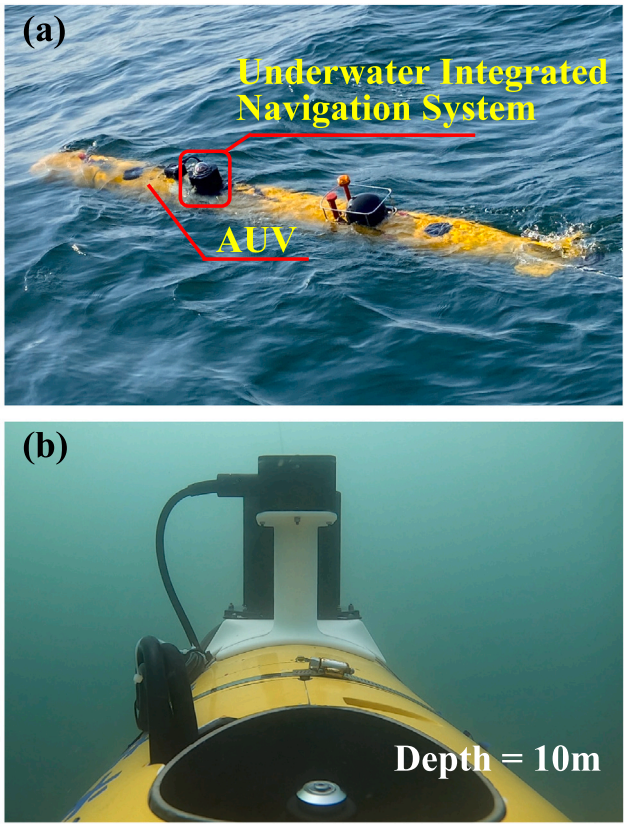

Fig. 6. The setup and environment at depth of 10 m in the dynamic sea trial.

Table 1
The features of navigation sensors.

Navigation sensors	Specifications
Polarimeter	View angle: 185° AoP perception accuracy: 0.61°(1σ)
Accelerometer	Random walk: 45(X,Y), 65(Z) μg/Hz Bias stability: 20 μg
Gyroscope	Random walk: 0.15°/$\sqrt{h}$ Bias stability: 8°/h

4.1. Underwater integrated navigation system overview

The structure, assembly units, and image of the underwater integrated navigation system are shown in Fig. 3. The navigation sensors consist a camera-based polarimeter (PHX050S-P), an inertial measurement unit (IMU), and a depthometer. A fisheye lens (FE185C057HA-1) with a view angle of 185° is equipped on the camera-based polarimeter. The industrial personal computer (IPC, NVIDIA Jetson NANO) is used for data processing and storage. The features of navigation sensors are given in Table 1.

4.2. Solar-tracking in static water-tank experiment

In order to evaluate the solar-tracking performance of the LIG method, the static experiment in a water tank was conducted in Qingdao, Shandong Province (36.175° N, 120.482° E) on July 31, 2021. The water tank with the size of $\phi 3 \times 1\text{m}^3$ provides the underwater environment. A box of milk (200 mm) was mixed in water to enhance the multiple scattering in the shallow water environment. The underwater polarization navigation system is fixed on a heading reference platform equipped with a set of double GNSS antenna system (heading accuracy: 0.1°). The solar-tracking reference is provided by solar-ephemeris [31].

In order to visually display the underwater downwelling light intensity field, the pseudocolor images of light intensity and LIG angle (γ) are shown in Fig. 4(a) and (b). The white short segments in Fig. 4(a) represent the unit vectors of LIG on different observation points. The majority of the unit vectors approximately point to the solar position. The distribution of LIG angle, as illustrated in Fig. 4(b), is exhibited in radiation pattern centered around the sun.

As can be seen from Fig. 4(c) and (d), the underwater downwelling light field patterns of AoP and LIG model are calculated by the method presented in Ref. [22] and LIG as given by Eq. (9), respectively. The white dot lines are guides to the eyes of the symmetry lines of the patterns. It is obvious that the symmetry line of AoP pattern is curved under turbid water. By contrast, the symmetry line of LIG pattern is still straight. This comparison confirms that the multiple scattering breaks the symmetry of AoP pattern, but has less effect on LIG.

The solar-tracking results of POL and LIG methods are visible in Fig. 5. It is obvious the there are deviations between the blue curves (calculated by POL method) and dark gray curves (Solar ephemeris) in Fig. 5(a) and (b). This is caused by the symmetry breaking of AoP pattern arising from water multiple scattering. The constant errors of LIG method are reduced obviously. The mean absolute error (MAE) is adopted to quantitatively evaluate the constant errors. The estimation accuracy improvements of solar azimuth and zenith of the LIG method are 42.42% (from 3.3° to 1.9°) and 55.17% (from 2.9° to 1.3°), respectively.

However, the fluctuation of LIG curves exhibits more intense than that of POL curves, which is ascribed to the enlarge of the measurement noise affection by gradient calculation. A conclusion can be drawn by the static experiment. The pattern of LIG is more robust than that of POL under the effect of multiple scattering. As a consequence, the LIG can reduce the constant errors of solar-tracking in comparison to the POL method in the multiple scattering underwater environments.

4.3. Orientation in dynamic sea trail

The sea trail on an AUV were conducted to verify the orientation performance in deep water. As shown in Fig. 6, the underwater navigation system was fixed on an AUV as a movement platform. The sea trail was performed in Weihai (122.06° E, 37.54° W), Shandong Province on September 3rd, 2021. The heading reference is provided by the integrated navigation of fiber-optic gyroscope-based INS/GNSS/DVL (Doppler velocity log) with the heading accuracy of 0.3°/h. The sea trial was conducted in two depths of 10 m and 15 m, respectively. The exposure time of the camera-based polarimeter was set as 700 μs in both of the two experiment depths.

Fig. 7 shows the submarine light fields of light intensity, AoP, DoP, and LIG in the depths of 10 m and 15 m. The 15m-depth DoP is obviously lower than 10 m-depth DoP. It indicates that multiple scattering caused by water depth has a significant depolarization effect. The low degree of polarization reduces the accuracy of polarization angle perception. In terms of the AoP distribution pattern, as is visible in Fig. 7(c) and (g), the symmetry lines of AoP patterns in 10 m and 15 m are curved. The phenomenon is analogous to that in the static water-tank test. Although the light intensity is attenuated by water depth as illustrated in Fig. 7(a) and (e). The symmetries of the corresponding LIG patterns in 10 m and 15 m is maintained under multiple scattering (see Fig. 7(d) and (h)). The LIG model exhibits stronger robustness as compared with the POL Rayleigh model in the deep-water environment.

Fig. 8 depicts the orientation comparison of POL/INS and the developed LIG/INS in the dynamic sea trail. In term of the results in 10 m depth, the deviation of heading estimated by POL/INS is larger than that estimated by LIG/INS. The improvement rate of orientation accuracy from POL/INS to LIG/INS is 55.56% (from 3.6° to 1.6°). More superior performance attained by LIG/INS in comparison to POL/INS exhibits in the depth of 15 m. From Fig. 8(c) and (d), the orientation

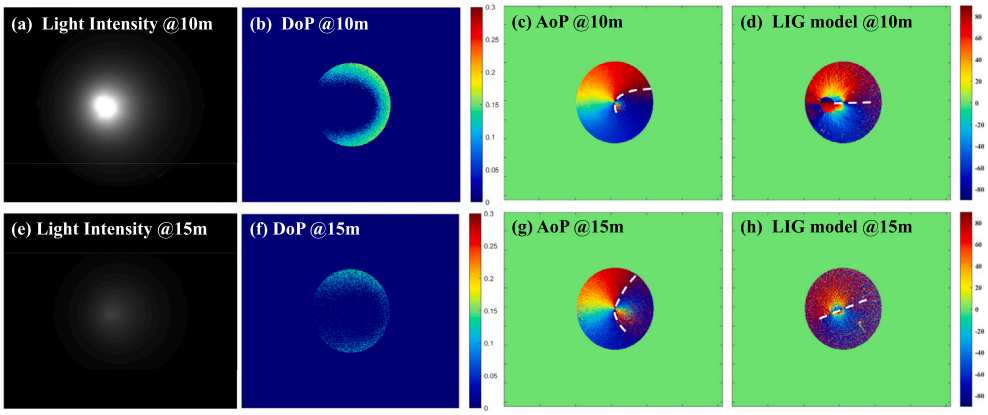

Fig. 7. The submarine light fields in the depths of 10 m and 15 m.

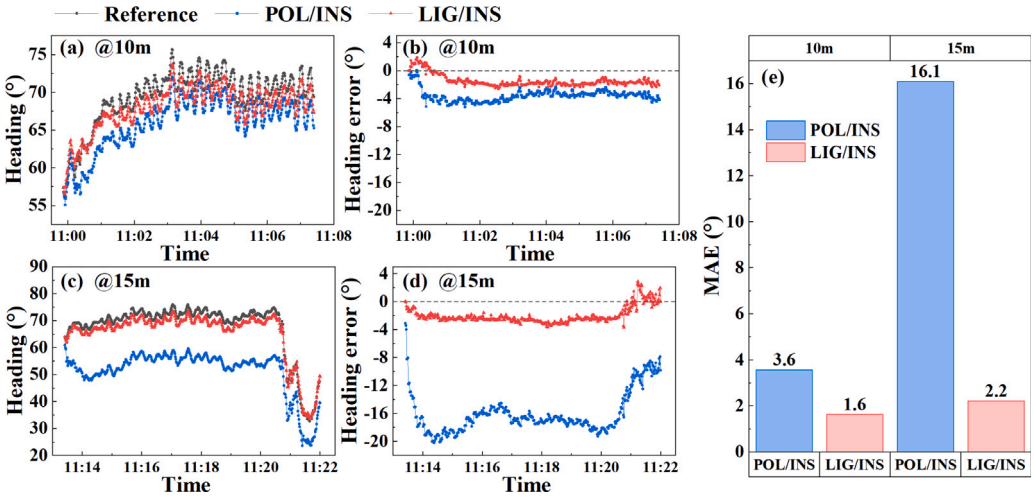

Fig. 8. Heading and heading error comparison between the POL/INS and LIG/INS in the depths of 10 m and 15 m.

accuracy is enhanced by 86.34% from 16.1° of LIG/INS to 2.2° of POL/INS. The distinction between the POL performances in the depths of 10 m and 15 m emphasizes that, the intensified water multiple scattering driven by deeper water enlarges the deviation between the idea Rayleigh model of POL and the real POL model. As a consequence, the orientation error of POL/INS is magnified. Benefiting from the robustness of the LIG in both optical information acquisition and distribution pattern, the integrated navigation system of LIG/INS has more powerful of environment suitability, especially for deeper water.

Remark 3. Under the experimental conditions mentioned in this work, the presented LIG-based orientation performed better than the traditional POL-based method. For deeper water, however, the limitation of LIG-based method appears due to the darker illumination. Low-light conditions increase the image noise that can be further enlarged by gradient calculation. In consequence, the performance of solar-tracking by LIG can suffer significantly. The improvements on camera-based polarimeter performance and image filter can be effective solutions to further enhance the environment suitability of submarine LIG-based navigation.

5. Conclusion

In this article, an autonomous orientation method based on submarine light intensity gradient field is developed, which improves the environment suitability of the navigation based on the underwater light field. The benefits of the proposed method include:

(1) The spatial information contained in the light intensity field is utilized by transforming the scalar field of light intensity to a vector field through the calculation of gradients. This navigation strategy owns the advantages of autonomy and free of error accumulation.

(2) The underwater light intensity owns the advantages in terms of the robustness in optical information acquisition and stability in distribution pattern. By means of LIG method, the water multiple scattering effects on polarization is avoided, while the constant deviations of POL-based solar-tracking are further eliminated. The LIG method demonstrates a higher level of environmental suitability, particularly in deep-water environments.

This improvements enable the navigation using submarine light field to be applied in deeper water. The LIG-based orientation provides an alternative strategy for underwater navigation.

The solar-tracking method LIG is only a basic theoretical model which is designed for an ideal underwater environment. The disturbance from the environment and sensors are not considered in this paper. In the future work, the interference (e.g., wave, turbidity, and sensor noise) will be considered into the model for better environmental suitability. Additionally, a better image denoising algorithm is required to reduce to the large STD of solar-tracking. At least, the fusion of underwater polarization field and light intensity field may be a viable option for better solar-tracking performance in the varied submarine environment.

CRediT authorship contribution statement

Pengwei Hu: Conceptualization, Methodology, Software, Writing – original draft. **Wenbin Liu:** Software optimization, Formal analysis, Manuscript proofreading. **Jian Yang:** Experiments implementation, Data curation. **Xiang Yu:** Writing – review & editing. **Lijun Xu:** Resource, Supervision. **Lei Guo:** Funding acquisition, Supervision.

Declaration of competing interest

The authors declare the following financial interests/personal relationships which may be considered as potential competing interests: Jian Yang reports financial support was provided by National Natural Science Foundation of China. Lei Guo reports financial support was provided by National Natural Science Foundation of China.

Data availability

The authors do not have permission to share data.

Acknowledgments

This work was supported by grants from the National Natural Science Foundation of China (Nos. 62227813, 62122007, 62388101, and 62073018).

All authors have read and agreed to the published version of the manuscript.

References

[1] Wang Y, Ma X, Wang J, Hou S, Dai J, Gu D, et al. Robust AUV visual loop-closure detection based on variational autoencoder network. IEEE Trans Ind Inf 2022;18:8829–38. http://dx.doi.org/10.1109/TII.2022.3145860.

[2] Allotta B, Caiti A, Chisci L, Costanzi R, Di Corato F, Fantacci C, et al. An unscented Kalman filter based navigation algorithm for autonomous underwater vehicles. Mechatronics 2016;39:185–95. http://dx.doi.org/10.1016/j.mechatronics.2016.05.007.

[3] Arunkumar G, Vachhani L. 3-d acoustic homing using 2-D asymptotes. Mechatronics 2020;70:102407. http://dx.doi.org/10.1016/j.mechatronics.2020.102407.

[4] Allotta B, Costanzi R, Fanelli F, Monni N, Ridolfi A. Single axis FOG aided attitude estimation algorithm for mobile robots. Mechatronics 2015;30:158–73. http://dx.doi.org/10.1016/j.mechatronics.2015.06.012.

[5] Wang B, Ma Z, Huang L, Deng Z, Fu M. A filtered-marine map-based matching method for gravity-aided navigation of underwater vehicles. IEEE/ASME Trans Mechatronics 2022;27:4507–17. http://dx.doi.org/10.1109/TMECH.2022.3159596.

[6] Wang Y, Ma X, Wang J, Wang H. Pseudo-3D vision-inertia based underwater self-localization for AUVs. IEEE Trans Veh Technol 2020;69:7895–907. http://dx.doi.org/10.1109/TVT.2020.2993715.

[7] Allotta B, Caiti A, Chisci L, Costanzi R, Di Corato F, Fantacci C, Fenucci D, Meli E, Ridolfi A. An unscented kalman filter based navigation algorithm for autonomous underwater vehicles. Mechatronics 2016;39:185–95. http://dx.doi.org/10.1016/j.mechatronics.2016.05.007.

[8] Shen C, Zhao X, Wu X, Cao H, Wang C, Tang J, Liu J. Multi-aperture visual velocity measurement method based on biomimetic compound-eye for uavs. IEEE Internet of Things Journal 2023. 1-1, https://dx.doi/10.1109/JIOT.2023.3324966.

[9] Liu X, Tang J, Shen C, Wang C, Zhao D, Guo X, Li J, Liu J. Brain-like position measurement method based on improved optical flow algorithm. ISA Trans. 2023;143:221–30. http://dx.doi.org/10.1016/j.isatra.2023.09.005.

[10] Patel RN, Cronin TW. Mantis shrimp navigate home using celestial and idiothetic path integration. Curr Biol 2020;30:1981–7.e3. http://dx.doi.org/10.1016/j.cub.2020.03.023.

[11] Daly IM, How MJ, Partridge JC, Temple SE, Marshall NJ, Cronin TW, et al. Dynamic polarization vision in mantis shrimps. Nature Commun 2016;7:12140. http://dx.doi.org/10.1038/ncomms12140.

[12] Sabbah S, Habib-Nayany MF, Dargaei Z, Hauser FE, Kamermans M, Hawryshyn CW. Retinal region of polarization sensitivity switches during ontogeny of rainbow trout. J Neurosci 2013;33:7428–38. http://dx.doi.org/10.1523/JNEUROSCI.5815-12.2013.

[13] Waterman TH. Polarization patterns in submarine illumination. Science 1954;120:927–32. http://dx.doi.org/10.1126/science.120.3127.927.

[14] Tang J, Wang Y, Zhao D, Guo X, Zhao J, Shen C, et al. Application of polarized light compass system on solar position calculation. Optik 2019;187:135–47. http://dx.doi.org/10.1016/j.ijleo.2019.04.129.

[15] Stürzl W, Carey N. A fisheye camera system for polarisation detectionon UAVs. In: Fusiello A, R Murino, Cucchiara, editors. Computer vision – ECCV 2012. Workshops and demonstrations. Berlin, Heidelberg: Springer Berlin Heidelberg; 2012, p. 431–40. http://dx.doi.org/10.1007/978-3-642-33868-743.

[16] Du T, Tian C, Yang J, Wang S, Liu X, Guo L. An autonomous initial alignment and observability analysis for SINS with bio-inspired polarized skylight sensors. IEEE Sens J 2020;20:7941–56. http://dx.doi.org/10.1109/JSEN.2020.2981171.

[17] Shen C, Wu X, Zhao D, Li S, Cao H, Zhao H, et al. Comprehensive heading error processing technique using image denoising and tilt-induced error compensation for polarization compass. IEEE Access 2020;8:187222–31. http://dx.doi.org/10.1109/ACCESS.2020.3028418.

[18] Liu J, Zhao D, Wang C, Yang J, Guo X, Tang J, et al. Attitude calculation method based on full-sky atmospheric polarization mode. Rev Sci Instrum 2019;90:015009. http://dx.doi.org/10.1063/1.5056195.

[19] Powell SB, Garnett R, Marshall J, Rizk C, Gruev V. Bioinspired polarization vision enables underwater geolocalization. Sci Adv 2018;4:eaao6841. http://dx.doi.org/10.1126/sciadv.aao6841.

[20] Dupeyroux J, Viollet S, Serres JR. An ant-inspired celestial compass applied to autonomous outdoor robot navigation. Robot Auton Syst 2019;117:40–56. http://dx.doi.org/10.1016/j.robot.2019.04.007.

[21] Zhang T, Yang J, Guo L, Hu P, Liu X, Huang P, et al. A bionic point-source polarisation sensor applied to underwater orientation. J Navig 2021;74:1057–72. http://dx.doi.org/10.1017/S0373463321000308.

[22] Hu P, Yang J, Guo L, Yu X, Li W. Solar-tracking methodology based on refraction-polarization in Snell's window for underwater navigation. Chin J Aeronaut 2022;35:380–9. http://dx.doi.org/10.1016/j.cja.2021.02.011.

[23] Dou Q, Du T, Wang S, Yang J, Guo L. A novel polarized skylight navigation model for bionic navigation with marginalized unscented Kalman filter. IEEE Sens J 2022;22:4472–83. http://dx.doi.org/10.1109/JSEN.2021.3139353.

[24] Wang J, Qian J, Guo L. An equivalent incident light model for multiple scattering and polarization neutral point of skylight. J Opt 2020;22:075603. http://dx.doi.org/10.1088/2040-8986/ab92b4.

[25] Hamaoui M. Polarized skylight navigation. Appl Opt 2017;56:B37–46. http://dx.doi.org/10.1364/AO.56.000B37.

[26] Edward C. Field guide to polarization. SPIE 2005. http://dx.doi.org/10.1117/3.626141.

[27] Groves PD. Principles of GNSS, inertial, and multisensor integrated navigation systems. In: IEEE aerospace and electronic systems magazine, vol. 30. 2nd ed. [book review]. 2015, p. 26–7. http://dx.doi.org/10.1109/MAES.2014.14110.

[28] Scaramuzza D, Martinelli A, Siegwart R. A toolbox for easily calibrating omnidirectional cameras. In: 2006 IEEE/RSJ international conference on intelligent robots and systems. 2006, p. 5695–701. http://dx.doi.org/10.1109/IROS.2006.282372.

[29] Horváth G, Varjú D. Underwater refraction-polarization patterns of skylight perceived by aquatic animals through Snell's window of the flat water surface. Vis Res 1995;35:1651–66. http://dx.doi.org/10.1016/0042-6989(94)00254-J.

[30] Quan W, Gong X, Fang J, Li J. Filters in navigation system. Berlin, Heidelberg: Springer Berlin Heidelberg; 2015, p. 53–73. http://dx.doi.org/10.1007/978-3-662-45159-5_3.

[31] Reda I, Andreas A. Solar position algorithm for solar radiationapplications. Sol Energy 2004;76:577–89. http://dx.doi.org/10.1016/j.solener.2003.12.003.

Pengwei Hu was born in Hebi, China, in 1990. He received the B.S. degree in electronic information engineering from the Henan University of Science and Technology, Luoyang, China, and the Ph.D. degree in control theory and control engineering from Beihang University, China, in 2013 and 2023 respectively. He is currently a Postdoctoral Research Fellow with the School of Instrumentation and Optoelectronic Engineering, Beihang University.

His research interests include bionic polarization navigation systems, autonomous integrated navigation systems with the application to underwater unmanned vehicle.

Wenbin Liu was born in Kunming, China, in 1999. He received the B.E. degree from the School of Automation Science and Electrical Engineering, Beihang University, Beijing, China, in 2021. He is currently a graduate student with the School of Automation Science and Electrical Engineering, Beihang University.

His current research interests include bionic polarization navigation, integrated navigation system, Information fusion method, and polarization vision.

Jian Yang was born in Chifeng, China, in 1987. He received the B.S. degree in control theory and control engineering from the Department of Automatic Control, Northeastern University, Shenyang, China, in 2011, and the Ph.D. degree in precision instrument and machinery from Beihang University, Beijing, China, in 2018. He is currently an Associate Professor with the School of Automation Science and Electrical Engineering, Beihang University.

His current research interests include bionic polarization navigation, autonomous navigation systems, and filter design with their applications to aerospace systems.

Xiang Yu received the B.S., M.S., and Ph.D. degrees in automation science and engineering from Northwestern Polytechnical University, Xi'an, China, in 2003, 2004, and 2008, respectively. He is currently a Professor with the School of Automation Science and Electrical Engineering, Beihang University, Beijing, China. He was a Post-Doctoral Research Fellow with the Department of Electrical and Computer Engineering, Western University, London, ON, Canada, and a Research Associate with the Department of Mechanical, Industrial and Aerospace Engineering, Concordia University, Montreal, QC, Canada. He has authored over 60 prestigious journal papers and a monograph, including IEEE Transactions, AIAA Journals, and Progress in Aerospace Sciences. His current research interests include safety control of unmanned aerial vehicles, autonomous navigation and control of hypersonic vehicles.

Prof. Yu was a recipient of the Recruitment Program for Young Professionals, Youth Science and Technology Award of Chinese Society of Aeronautics and Astronautics, the Best Paper and Best Paper Finalist at international conferences. He has also served as the Associate Editor of Asian Journal of Control, Associate Editor of Journal of Intelligent & Robotic Systems, Associate Editor of Chinese Journal of Aeronautics, Program Co-Chair, Invitation Chair, and IPC Member of several academic conferences.

Lijun Xu received the B.Sc., M.Eng., and Ph.D. degrees in electrical engineering and instrumentation from Tianjin University, Tianjin, China, in 1990, 1993, and 1996, respectively.

From 1997 to 2001, he was an Associate Professor with Tianjin University. From 2002 to 2006, he was a Research Fellow with the University of Greenwich, London, U.K., and the University of Kent, Canterbury, U.K., and a Higher Scientific Officer with The Institute of Cancer Research, London, Sutton, U.K. He is currently a Professor and the Dean of the School of Instrumentation and Optoelectronic Engineering, Beihang University, Beijing, China. He has authored or coauthored more than 200 publications. His current research interests include tomographic imaging, scanning imaging, and dynamic process monitoring.

Dr. Xu is a Distinguished Young Scholar awarded by the National Natural Science Foundation of China (NSFC). He received the First-Class Invention Award from the Ministry of Education Technology and the First-Class Award from the Chinese Instrument Society Science and Technology in 2012, 2012, and 2014. He was elected as a Chang-Jiang Scholar Program Professor and a National High-Level Personnel of Special Support Program by the Ministry of Education and the Ministry of Organization, China, in 2014 and 2016, respectively.

Lei Guo was born in Qufu, China, in 1966. He received the B.S. degree in fundamental mathematics and M.S. degree in operational research and cybernetics from Qufu Normal University, Qufu, China, in 1988 and 1991, respectively, and the Ph.D. degree in control engineering from Southeast University, Nanjing, China, in 1997.

From 1991 to 1994, he was a Lecturer with Qingdao University, Qingdao, China. From 1997 to 1999, he was a Postdoctoral Fellow with Southeast University. From 1999 to 2000, he was a Research Fellow with IRCCyN, Nantes, Frances. From 2000 to 2003, he was a Research Fellow with the University of Glasgow, Glasgow, U.K.; Loughborough University, Loughborough, U.K.; and the University of Manchester Institute of Science and Technology, Manchester, U.K. In 2004, he joined the Institute of Automation, Southeast University, as a Professor. In 2006, he became a Professor with the School of Instrumentation and Opto-Electronics Engineering, Beihang University, Beijing, China, where he is currently with the School of Automation Science and Electronic Engineering. He has published more than 260 papers and served as an Editor for five journals. His research interests include robust control, stochastic systems, fault detection, filter design, and nonlinear control with their applications to aerospace systems.

Prof. Guo is an Awardee of the National Science Fund for Distinguished Young Scholars of China and a Changjiang Distinguished Professor of the Ministry of Education of China.